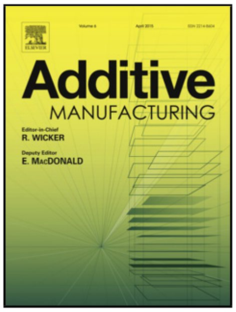

Title: Tailoring selective laser melting process for titanium drug-delivering implants with releasing micro-channels

Authors: Hany Hassanin, Laurane Finet, Sophie C. Cox, Parastoo Jamshidi, Liam M. Grover, Duncan E.T. Shepherd, Owen Addison, Moataz M. Attallah

PII: S2214-8604(17)30577-8
DOI: https://doi.org/10.1016/j.addma.2018.01.005
Reference: ADDMA 270

To appear in:

Received date: 3-12-2017
Revised date: 26-1-2018
Accepted date: 26-1-2018

Please cite this article as: { https://doi.org/

Tailoring Selective Laser Melting Process for Titanium Drug-Delivering Implants with Releasing Micro-Channels

Hany Hassanin[1,2], Laurane Finet[2], Sophie C. Cox[3], Parastoo Jamshidi[2], Liam M. Grover[3], Duncan E.T. Shepherd[4], Owen Addison[5], Moataz M. Attallah[2]

[1] School of Mechanical and Aerospace Engineering, Kingston University, London, SW15 3DW, UK
[2] School of Metallurgy & Materials, University of Birmingham, Edgbaston, B15 2TT, UK
[3] School of Chemical Engineering, University of Birmingham, Edgbaston, B15 2TT, UK
[4] Department of Mechanical Engineering, School of Engineering, University of Birmingham, Edgbaston, B15 2TT, UK
[5] School of Dentistry, University of Birmingham, Edgbaston, B15 2TT, UK

Graphical abstract

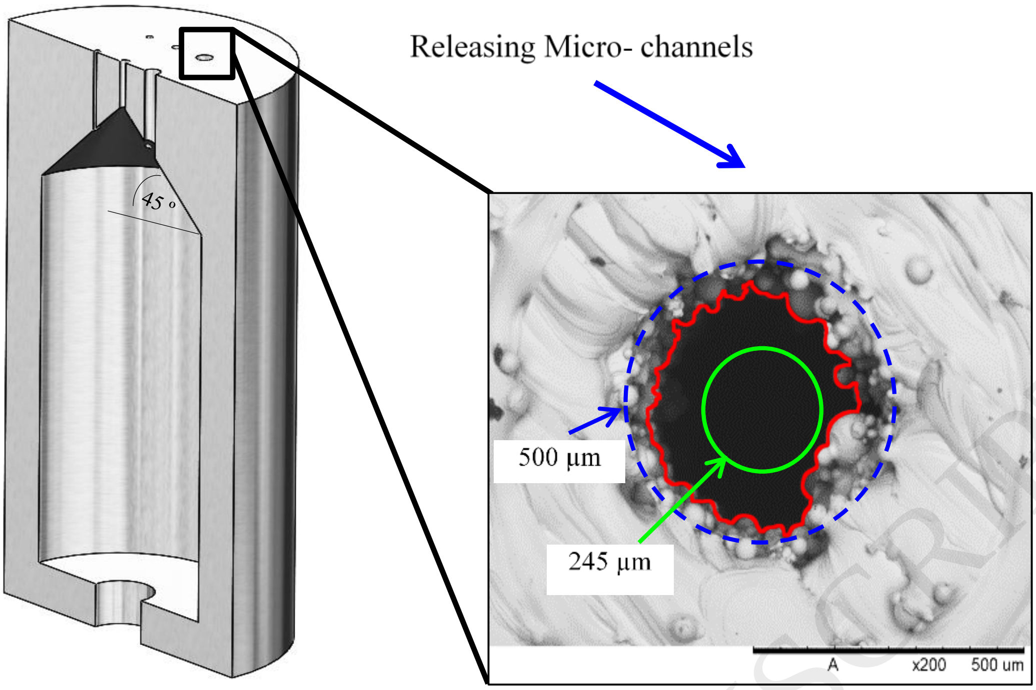

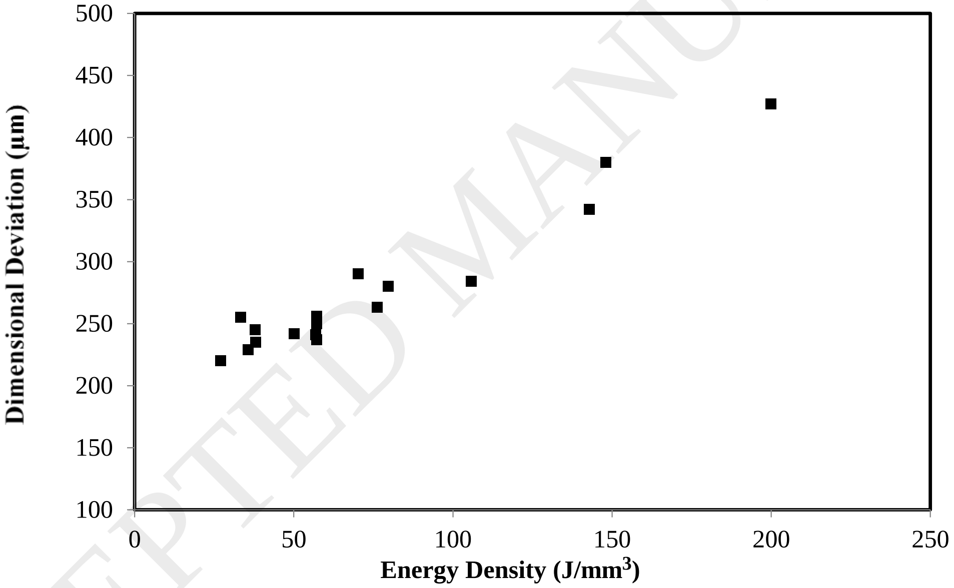

Abstract

The use of drug-delivering implants can minimise implant failure due to infection through a controlled medication release into the surrounding tissues. In this study, selective laser melting (SLM) was employed to manufacture Ti-6Al-4V samples, with internal reservoirs and releasing Micro-channels (MCs) to simulate what could be a drug-delivering orthopaedic or dental implant. Investigations were performed to optimise the design and SLM process parameters required to create the releasing MCs with minimum dimensional deviation to allow a controlled dosing of the drugs, while considering the process impact on the surface roughness and porosity of the builds. The build orientation, internal contour spacing, and laser process parameters were varied to assess their effect on the resolution of the MCs with diameters of ~200-500 µm. It was found that, vertically oriented channels were found to have the least dimensional deviation from the target dimensions compared with horizontally-oriented or inclined channels. The dimensional deviation of the MCs was found in range of 220-427 µm, while the horizontal surface roughness (R_a) was in range of 1.46-11.46 µm and the vertical surface roughness (R_a) was in range of 8.5-13.23 µm when applying energy density varying from of 27-200 J/mm^3. It was found that, there was a clear correlation between the energy density with both dimensional deviation and horizontal surface roughness, while no correlation was found for the vertical' surface roughness. The study identified the optimum conditions to manufacture drug-delivering metallic implants, creating hollow samples with releasing MCs equivalent diameter of ~271 µm, horizontal surface roughness (R_a) of 4.4 µm, vertical surface roughness of (R_a) 9.2 µm, and build porosity of 1.4% using an internal contour of 150 µm and energy density of 35.7 J/mm^3.

Keywords: Selective Laser Melting; Titanium Alloys; Medical Implants; Surface Roughness

1. Introduction

The demand for implantable medical devices is being driven by population growth to over 7 billions, the ageing population in the developed countries, and improvement in the healthcare in developing countries [1]. Medical technologies that improve healthcare have become abundant, especially for traumatic injury patients or those suffering from chronic illnesses. The global sales of biomedical implants are estimated to reach $116 billion by 2022, with an annual growth rate of 7.1% from 2016 to 2022. The highest revenue-generating market in this sector is orthopaedic implants [2]. Surgeries of this type of implants have been well-established for decades, and have improved the medical conditions of patients who suffer from bone and joint problems. However, 10% of these surgeries fail [3], mainly as a result of implant failure due to infection, fibrous encapsulation, and stress shielding. Among the aforementioned reasons, implant infections account for more than 20% of orthopaedics implant failures. Although surgery rooms, equipment, and implants are sterilised, infections still do happen. If a serious infection develops, revision surgery will be needed to remove the infected implant and implant a new one [4, 5].

Infections in implants can be prevented through local delivery of drugs embedded within an implant (e.g. antibiotics, anti-inflammatory, pain relief, or wound-healing agents). Recently, antibiotics have been embedded in bone cement [6, 7]. Nonetheless, using this approach, there is no control over the drug release rates, which can either result in overdosing (i.e. toxic), or under dosing (i.e. ineffective). Furthermore, prolonged administration of an antibiotic may develop antibiotic resistance. An alternative approach to reduce or control implants-associated infections is to embed the drug within a reservoir inside the implant itself [7, 8]. Although, drug-eluting or drug-loaded orthopaedic implants show promising results, to date, there is no well-established manufacturing process nor clinical practice has been made for this approach, hence, further research is needed [9-12]. Furthermore, the use of customised orthopaedic implants tailored to patients' medical condition, bot mechanically and therapeutically, is an attractive approach to achieve better patient outcomes.

Additive Manufacturing (AM) is a game changer for several applications especially in the medical sector. Compared to other manufacturing processes, AM offers lower production costs for customised low-batch components, with reduced material waste and shorter lead-times when compared to conventional machining [13-15]. However, perhaps the greatest advantage, is that AM enables significant design freedom, allowing the manufacture of complex-shaped parts with that would be impossible to manufacture by conventional means [16-18]. Selective laser melting (SLM) is an AM process that involves the use of a laser beam to selectively melt powder layers based on a designed CAD model, resulting in fusing a series of powder layers on top of each other under an inert atmosphere to create a 3D component [19].

Titanium and its alloys have been widely used in orthopaedics and dental applications over the past few decades due to their excellent biocompatibility, superior mechanical and fatigue strength [20]. One particular alloy, Ti-6Al-4V, has been used for orthopaedic implants for several decades. The uniqueness of this alloy is good corrosion resistance, an ability to integrate with native tissues and a Young's modulus closer to bone than stainless steels or CoCr alloys [21, 22]. AM of Ti-6Al-4V orthopaedic implants has been studied by several research groups [23, 24]. Bracke *et al.* [25] studied the use of electron beam melting (EBM) as an enabling technology to produce complex and functional Ti-6Al-4V cellular implants for the orthopaedic, dental, and maxillofacial remits, using the flexibility offered by AM to customise the implants according to patient’s geometries using Computed Tomography (CT) data. They were able to control the stiffness of the implant by manipulating the density of the cellular structures. Others such as, Wicker *et al.* have focused on the mechanical properties of Ti-6Al-4V cellular knee implants manufactured by EBM [26], whereas Sun *et al.* used SLM to create porous medical implant scaffolds using CT data, optimising the density of the cellular structure to control bone-implant interface instability and bone resorption [27]. Okabe *et al.* studied the fatigue life of Ti-6Al-4V alloy fabricated by direct-energy EBM, Direct Laser Deposition (DED), and conventional manufacturing techniques for dental implants. They found that the DED Ti-6Al-4V parts show better fatigue life than the EBM, but a shorter fatigue life than the rolled Ti-6Al-4V samples [28]. Despite the wealth of work on AM of medical implants, no work is available on exploiting the design freedom of AM to manufacture drug-delivering metallic implants, which is the subject of the present investigation.

In order to utilise SLM to produce a drug-delivering implant, it is essential that drug release kinetics may be controlled. Assuming that the drug is going to be contained within an internal cavity (reservoir), the delivering channels may be manipulated to enable the prediction of the release rates, while being dense and biocompatible in order to integrate with the body tissues [29]. For instance, residual porosity even with small amount can degrade the mechanical properties of the components, especially the fatigue. Therefore, the majority of recent AM research has been focused on the optimisation of the process parameters towards achieving near full density [30-34]. On the other hand, the surface topology of an implant has an important effect on the healing and integration with surrounding native tissues. Therefore, efforts have been made to control surface roughness of AM-fabricated implants in order to improve integration, particularly at the interface. In particular, surface topology plays a very important role in cell differentiation and attachment [35, 36]. To elicit a favourable biological response it has been recommended that the optimum surface roughness for orthopaedic implants should to be in the range R_a= 1–2 μm [37].

This work focuses on using SLM to develop drug-delivering Ti-6Al-4V implants, with MCs that may be manipulated to control therapeutic release kinetics. The design concept of the implant is presented as a simplified cylindrical implant with a central reservoir and surface connected MCs to elute the drug within the surrounding 3D environment. The releasing MC have been designed with different sizes and orientations with respect to the SLM build direction; vertical, inclined and horizontal channels. A design of Experiment (DoE) approach was employed to study the influence of the SLM process parameters on the resolution of the MC, as well as the surface roughness and the density of the implants, which in turn are critical to implant performance.

2. Experimental

2.1 Design of the implant samples

The design of the implants are shown in Figure 1. The samples were designed as hollow and cylindrical (10 mm in diameter, and 20 mm in height) to allow the characterisation of the internal structure using CT. A hole with a diameter of 2 mm was positioned at the top of the samples for the injection of the drug. In addition, a cavity with a diameter of 7 mm and a height of 13.5 mm was designed with various channel orientations connected to the surface extremes for drug delivery. One of the geometrical constraints of SLM is overhanging features, where a slightly inclined or flat feature is built directly on loose powder. This may lead to build distortions and failure of the build. This can be avoided by using an internal support structure to avoid the collapse of the structure being built. Another solution of this problem is to use self-supporting structures. The recommended angle for self-support structures depends on the material and the process parameters but in most cases, it is about 45˚. Therefore, the horizontal surface of the reservoir has been designed using a conical shape with a 45º inclined angle to enable the production of a self-supporting surface. As SLM induces anisotropic microstructural, geometrical, and mechanical properties the releasing MCs were built using different orientations to identify which was optimal in terms of feature resolution and geometrical accuracy. Cylindrical 500 µm, 300 µm, and 200 µm MCs were investigated. All of the samples were built on the same build substrate in the same batch. The orientation of the MCs with respect to the build direction defined the MCs type (vertical, horizontal, or inclined). Figure 1 shows a vertical cross-sectional view with the cylindrical samples created with horizontal, vertical and inclined MCs. The MCs direction parallel to the SLM build direction were defined as vertical (Figure 1a), whereas those perpendicular to the SLM build direction were defined as horizontal (Figure 1b), and those inclined at a 45º angle to the SLM build direction were defined as inclined (Figure 1c).

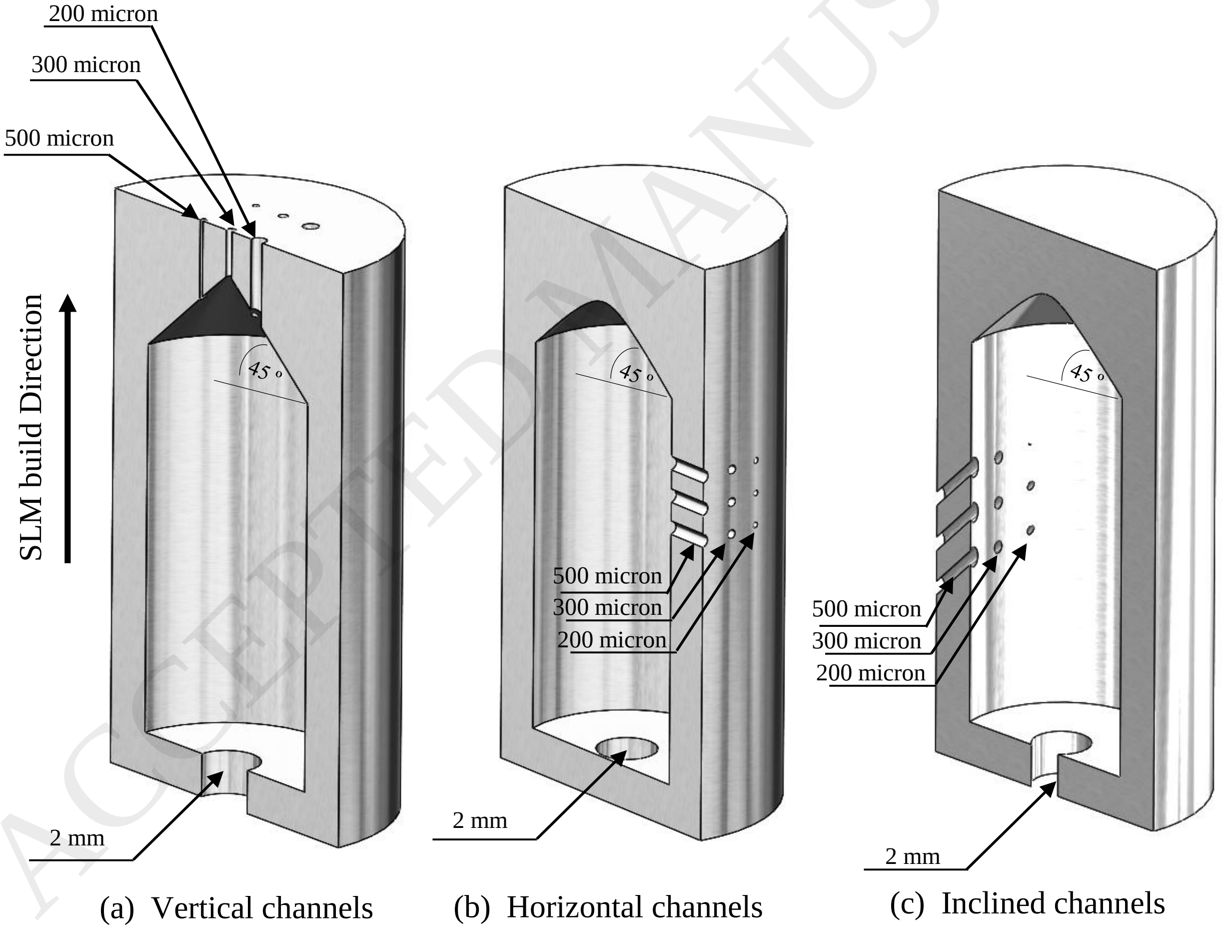

(a) Vertical channels (b) Horizontal channels (c) Inclined channels

Figure 1: Sectional view of the hollow cylindrical samples with (a) vertical channels, (b) horizontal channels, and (c) inclined channels.

2.2 Design of Experiment

In this study, the design of experiment (DoE) was carried out using the response surface methodology. DoE was used to find a relationship between the laser input parameters in terms of power (100-200 W), scan speed (500-3000 mm/s), and hatch spacing (30-120 µm), with the output parameters in terms of MCs dimensional deviation, surface roughness, and solid part density. This is to optimise the process responses towards achieving a minimum dimensional deviation and a target surface roughness in a range of R_a= 1–2 µm [37].

The volumetric energy density (Ψ), an empirical parameter, was used in this study to assess the influence of SLM parameters on the degree of consolidation, surface roughness, and geometrical accuracy of the samples, as given by [38].

$$\Psi = \frac{P}{\nu . h . t} \tag{1}$$

where P, ν, h, and t are the laser power (W) and scan speed (mm/s), h is scan spacing (mm), and t is the powder layer thickness (mm), respectively. The generated matrix of the process parameters of 17 samples and the corresponding energy density is shown in Table 1.

Table 1: The matrix of the investigated parameters

Samples	Laser Power (W)	Scan Speed (mm/s)	Hatch Spacing (µm)	Energy Density (J/mm^3)
1	125	2375	97.5	27
2	200	1750	75	76.2
3	175	1125	52.5	148.1
4	125	2375	52.5	50.1
5	150	1750	120	35.7
6	150	500	75	200
7	125	1125	52.5	105.8
8	175	2375	97.5	37.8
9	150	1750	75	57.1
10	125	1125	97.5	57
11	150	1750	30	142.9
12	175	1125	97.5	79.8
13	150	3000	75	33.3
14	150	1750	75	57.1
15	150	1750	75	57.1
16	175	2375	52.5	70.1
17	100	1750	75	38

2.3 Selective Laser Melting

A M2 Cusing SLM system (Concept Laser, Germany) equipped with an Nd:YAG laser with a wavelength of 1075 nm, a constant beam spot size of 70 µm, a laser power of 200 W and a speed up to 4000 mm/s was used to build the implant model in an Argon atmosphere (<100 ppm). Gas atomised Ti-6Al-4V powder in the 20-50 µm range (supplied by TLS Technik, Germany was used in the study. All the samples were built using a layer thickness of 20 µm. The scanning strategy and geometry parameters, especially the use of internal and/or external contours, are other SLM associated factors. As shown in Figure 2, an 'island scanning strategy' was used, whereby the build is partitioned into squares (islands). The islands are scanned randomly, with and the scan direction shifting by 90° between neighbouring islands, and moving by 1 mm in both the X and Y-directions in successive layers. The island size set for all experiments was 5 mm. After scanning all the islands in a powder layer, a contour scan is made around the part edges (using the same laser power and scan speed) to improve the part surface finish and resolution. The effect of the internal contour (IC) spacing from the hole edge was considered when studying the MCs dimensional deviation. Three different IC spacing were used: 25 µm, 150 µm, and 300 µm (Figure 2).

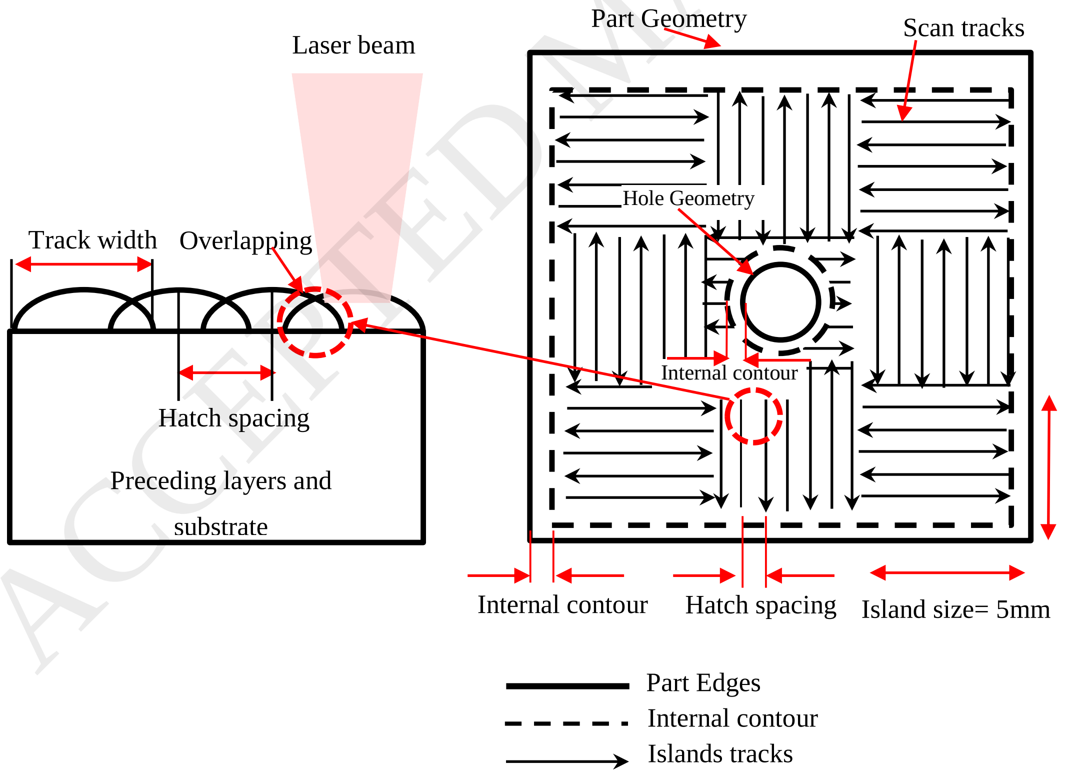

Figure 2: An illustration of the scanning strategy and internal contour during SLM.

2.4 Characterisation

2.4.1 Qualitative and Quantitative Tests of the Micro-Channels

A screening qualitative test was carried out to identify those samples with blocked MCs. For this qualitative test, the cylindrical samples was subjected to a pressurised air stream, immersed underwater and visually inspected for any air bubbles leaking from the samples. MCs that did not show air bubbles coming through them were noted as blocked and were excluded from further examination. Quantitative measurements were performed to calculate the dimensional deviation from the designed MCs diameter/area using a Hitachi TM300 desktop SEM and image analysis using ImageJ®.

The effective diameter (D_{eff}) is a term used to represent irregular holes in fluid flow scenarios using its wetted circumference (C) and area (A). ImageJ was used to fit an approximate polynomial curve through the opening of each micro-channel imaged using the SEM to calculate the circumference and the area of the fitted curve. The samples measurement was done in triplicate and the average values were recorded, representing D_{eff} as:

$$\mathrm{D}_{eff} = 4\frac{\mathrm{A}}{\mathrm{C}} \tag{2}$$

The dimensional deviation was calculated as the difference between the CAD designed target diameter and the effective diameter of the MCs using:

$$\text{Dimensional Deviation} = \text{Designed diamter} - (D_{eff}) \tag{3}$$

2.4.2 Surface Roughness

The surface roughness of the samples was measured using a SurrCorder SE1700 system, with a stylus tip radius of 2 µm. Normal mode of measurement was applied with an increment of 313 µm. The measure length was 2.5 mm, with a zero-prelength. Both the measure and return speeds were set to 0.1 mms^{-1}. Three measurements were carried out for the horizontal and vertical surfaces of each sample.

2.4.3 Micro-computer tomography

The implant models were scanned using a Skyscan1172 micro-computer tomography (micro-CT) system (Bruker, Belgium), with 80 kV maximum X-ray energy, 8 W beam power, 2000 ms exposure per projection, aluminium and copper filters, and 5.95 µm pixel size. Porosity analysis of the implant model with inclined pore channel design was conducted using *CTAn* (version 1.15.4.0, Bruker) software. Briefly, a circle was fitted to the external edges of the cylinder to create a region of interest (ROI). The ROI was interpolated across 100 slices positioned in the middle of the longitudinal axis of the sample volume to create a volume of interest (VOI). A global thresholding was applied to create a binary image, which was then filtered to remove noise. A ROI shrink wrap function used to define the sample extremities. 3D analysis was run over this VOI to determine total, open, and closed porosity as well as the size distribution of open and closed pores. Micro-CT values of porosity were compared with those obtained from Archimedes density measurements.

3. Results and Discussion

3.1 Dimensional Accuracy of the Micro-Channels

3.1.1 Effect of the Internal Contour

For its importance on the resolution and accuracy of MCs, the effect of the IC spacing was studied. An example of the results is listed in Table 2 and Figure 3.

Table 2: Effective diameters for the MCs built using different internal contours.

IC Spacing (µm)	D_{eff} (μm)		
	500 µm MCs	300 µm MCs	200 µm MCs
25	157	Blocked	Blocked
150	280	111	Blocked
300	245	78	Blocked

Figure 3 shows SEM images of the vertical MCs with respect to the IC spacing for samples built using 27 J/mm^3. As shown, the IC tracks can be clearly identified around the micro-channel. The width of the IC track was found to be in range of 150 µm -200 µm. For the MCs produced with a target diameter of 500 µm using an IC spacing of 25 µm, the effective diameter was found to be 157 µm, (Figure 3-a). On the other hand, when IC spacing of 150 µm was used, the effective diameter was found to be 280 µm, Figure 3-b. Finally, when IC spacing of 300 µm was employed, the effective diameter of the 500 µm MCs were found to be 245 µm, see Figure 3-c. Looking at Figure 3-d,e,f, the MCs with a target diameter of 300 µm were blocked when using IC spacing of 25 µm. while the effective diameters were found to be 111 µm and 78 µm when IC spacing of 150 µm and 300 µm were used, respectively. Finally, and although a low laser energy was used in these samples, the MCs built with target diameter of 200 µm were all blocked regardless to the IC spacing, see Figure 3 g,h,i.

In general, the track width IC (melt pool) depends on a number of factors, including the material thermo-physical characteristics and process parameters. Wider scan track width is typically developed when higher laser power and lower laser scanning speed are used [39]. It can be clearly noted that using IC spacing smaller than the track width results in a smaller MC. When the IC takes place at a distance closer to the edge of a micro-channel, a reduction in the diameter of the MCs was obtained for MCs with a target diameter of 500 µm, while blocking MC with a target diameter ≤ 300 µm. Using IC spacing similar to the track width results in samples with larger effective dimeter, and hence minimal dimensional deviation. Furthermore, dimensional deviation becomes larger when the MCs diameter gets < 200 µm, as there is a good chance for the MCs to be clogged with loose or partially melted powder. As a result, IC spacing of 150 µm was used in the following experiments as it produced samples with the least dimensional deviation.

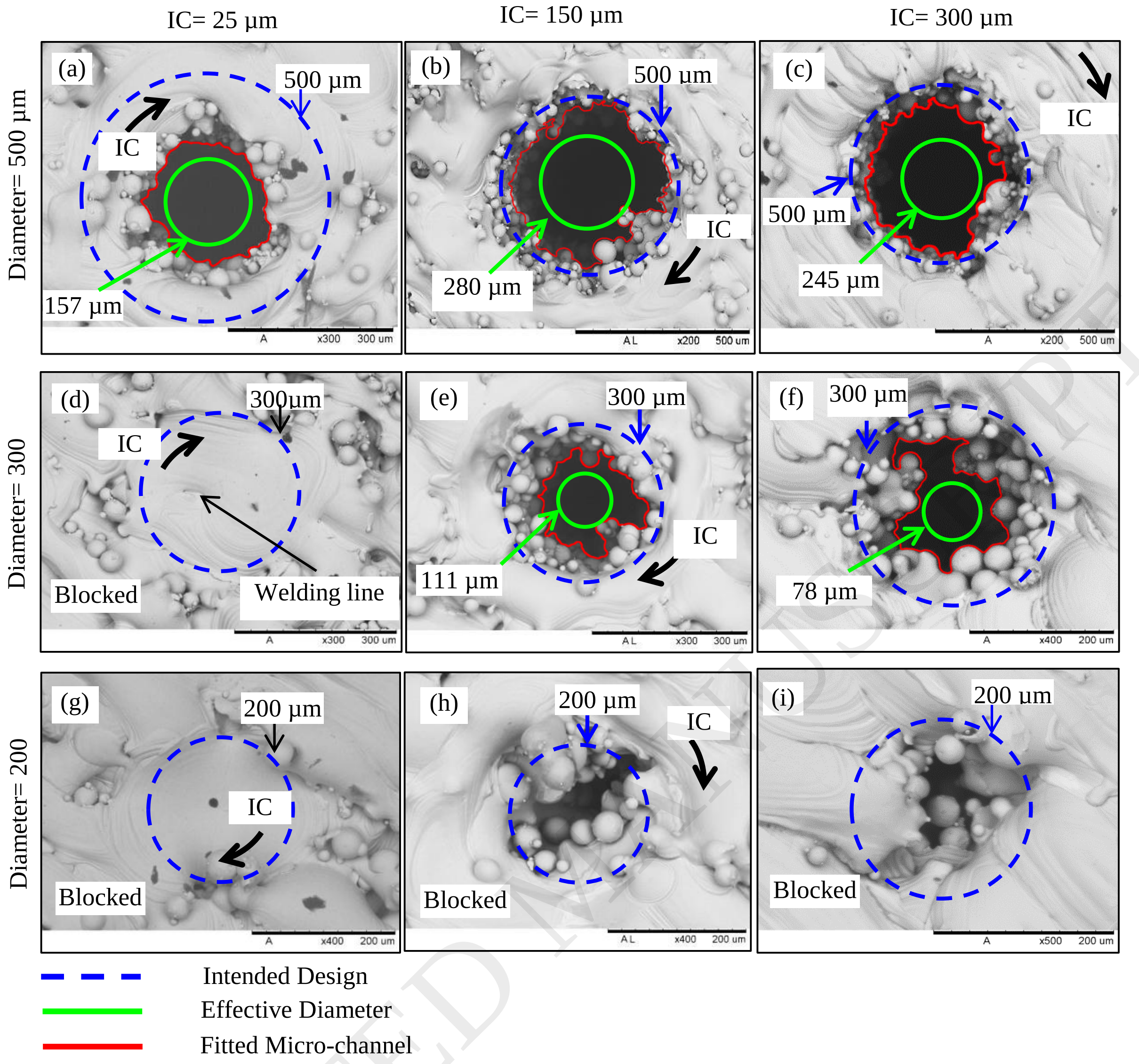

Figure 3: An example of SEM images of vertical MCs built with (a) D = 500 µm, IC spacing 25 µm, (b) D = 500 µm, IC spacing 150 µm, (c) D = 500 µm, IC spacing 300 µm, (d) D = 300 µm, IC spacing 25 µm, (e) D = 300 µm, IC spacing 150 µm, (f) D = 300 µm, IC spacing 300 µm, (g) D = 200 µm, IC spacing 25 µm, (h) D = 200 µm, IC spacing 150 µm, (i) D = 200 µm, IC spacing 300 µm.

3.1.2 Effect of Build Orientation

The effect of build orientation on the MCs was investigated for the samples built using IC spacing of 150 µm. The quantitative and qualitative measurements for all the specimens are presented in Table 3. The effective diameters were carried out on samples built with vertical, inclined, and horizontal MCs. In general, it can be noticed that the effective diameter of all channels is smaller than the target diameter regardless to the process parameters or IC spacing. For MCs built vertically with a target diameter of 500 µm, samples 1, 5 and 17 show the highest effective diameters, within a range of 265-280 µm. On the other hand, the lowest effective diameter was found for sample 6. The values of the effective diameter of this sample was found 73 µm. On the other hand, for horizontal MCs built with a designed diameter of 500 µm, samples 17 and 1 show the smallest effective diameters of 204 µm and 195 µm, respectively. As for the inclined MCs with intended design diameter of 500 µm, samples 5 and 17 show the best effective diameter of 225-238 µm. Furthermore, MCs built with intended design diameter of 300 µm found blocked when the build direction is horizontal or inclined. Samples built vertically shows through holes except for samples 3, 6 and 11. Finally, samples built with MCs size of 200 µm were found blocked regardless to the build direction or the laser energy input. In summary, the best effective diameters were found for samples 1, 5 and 17.

Table 3: Effect of building direction on the effective diameter of the MC.

Run	Effective diameters, µm								
	500 µm MCs			300 µm MCs			200 µm MCs		
	V	H	I	V	H	I	V	H	CB
1	280	195	116	111	B	B	B	B	B
2	237	B	B	76	B	B	B	B	B
3	120	B	B	B	B	B	B	B	B
4	258	180	113	97	B	B	B	B	B
5	271	188	225	143	B	B	B	B	B
6	73	B	B	B	B	B	B	B	B
7	216	B	142	71	B	B	B	B	B
8	255	132	135	73	B	B	B	B	B
9	244	117	147	106	B	B	B	B	B
10	259	137	175	113	B	B	B	B	B
11	158	B	B	B	B	B	B	B	B
12	220	B	95	65	B	B	B	B	B
13	245	162	195	47	B	B	B	B	B
14	263	138	153	99	B	B	B	B	B
15	250	127	146	109	B	B	B	B	B
16	210	B	B	81	B	B	B	B	B
17	265	204	23	128	B	B	B	B	B

B Blocked, V vertical, H horizontal, I Inclined

3.2 Effect of Process Parameters on Dimensional Deviation and Surface Roughness

Statistical analysis of the collected DoE results was carried out to study the effect of the process parameters (laser power, scan speed, hatch spacing) on the response factors (dimensional deviation of the releasing MCs, and horizontal and vertical surface roughness). The dimensional deviation of the MCs data was presented using the data collected for the vertical MCs with a designed diameter of 500 µm as they all were through holes, Table 4.

Table 4: Matrix building parameters and responses

Samples	Energy Density (J/mm^3)	Dimensional Deviation (μm)	Horizontal R_a (μm)	Side R_a (μm)
1	27	220	11.46	11.945
2	76.2	263	3.86	10.94
3	148.1	380	7.175	10.53
4	50.1	242	5.455	11.165
5	35.7	229	4.36	9.24
6	200	427	1.455	10.205
7	105.8	284	3.825	9.62
8	37.8	245	8.075	13.23
9	57.1	256	5.525	10.83
10	57	241	4.81	8.9
11	142.9	342	2.63	9.425
12	79.8	280	5.35	8.5
13	33.3	255	8.43	11.005
14	57.1	237	7.04	9.915
15	57.1	250	6.555	8.75
16	70.1	290	6.415	11.455
17	38	235	7.39	9.44

Each of the response surfaces is a function of laser power, scan speed and hatch spacing using the following regression equation:

$$\begin{aligned}(Responce) \quad &= b_0 + \ b_1\, Power\ (W) + \ b_2\, speed\ \left(\frac{mm}{s}\right) + b_3\, Hatching\ Space (\mu m) \quad + \\ &b_4\, power\ (W)\ power\ (W) + b_5\, speed\ \left(\frac{mm}{s}\right) * speed\ \left(\frac{mm}{s}\right) + \\ &b_6\ \ Hatching\ Space\ (\mu m)\ \ Hatching\ Space\ (\mu m)\ +\ b_7\, power\ (W)\ speed\ \left(\frac{mm}{s}\right) + \\ &b_8\, power\ (W) *\ Hatching\ Space\ (\mu m)\ + \\ &b_9\, speed\ \left(\frac{mm}{s}\right)\ Hatching\ Space\ (\mu m) \end{aligned} \tag{5}$$

where b_i are responses coefficients that calculated based on the main and interaction responses of the process parameters. The values of the coefficients for the dimensional deviation of the releasing MCs, horizontal and vertical surface roughness are shown in Table 5. The model fit (R^2 value) of the models were found the highest of 0.93 and 0.82 for the dimensional deviation and horizontal roughness, respectively. On the other hand, the R^2 value was 0.61 for the vertical roughness indicating a less precise model.

Table 5: Response surface model coefficients for dimensional deviation, horizontal surface roughness, and vertical surface roughness.

Coefficient	Dimensional deviation (µm)	Horizontal surface roughness (R_a)	Vertical surface roughness (R_a)
b_o	369	-32.7	19.6
b_1	2.87	0.25	- 0.07
b_2	- 0.24	7.0 x E^{-3}	- .6 x E^{-3}
b_3	- 2.43	0.33	- 0.072
b_4	- 3 x E^{-5}	- 1.98 x E^{-4}	2.30 x E^{-4}
b_5	5.9 x E^{-5}	- 1.0 x E^{-6}	1.0 x E^{-6}
b_6	1.8 x E^{-2}	- 1.29 x E^{-3}	- 1.4 x E^{-4}
b_7	- 4.96 x E^{-4}	- 5.1 x E^{-5}	2 x E^{-6}
b_8	- 1.78 x E^{-2}	- 1.590 x E^{-3}	1.09 x E^{-4}
b_9	6.76 x E^{-4}	7.6 x E^{-5}	4.3 x E^{-5}

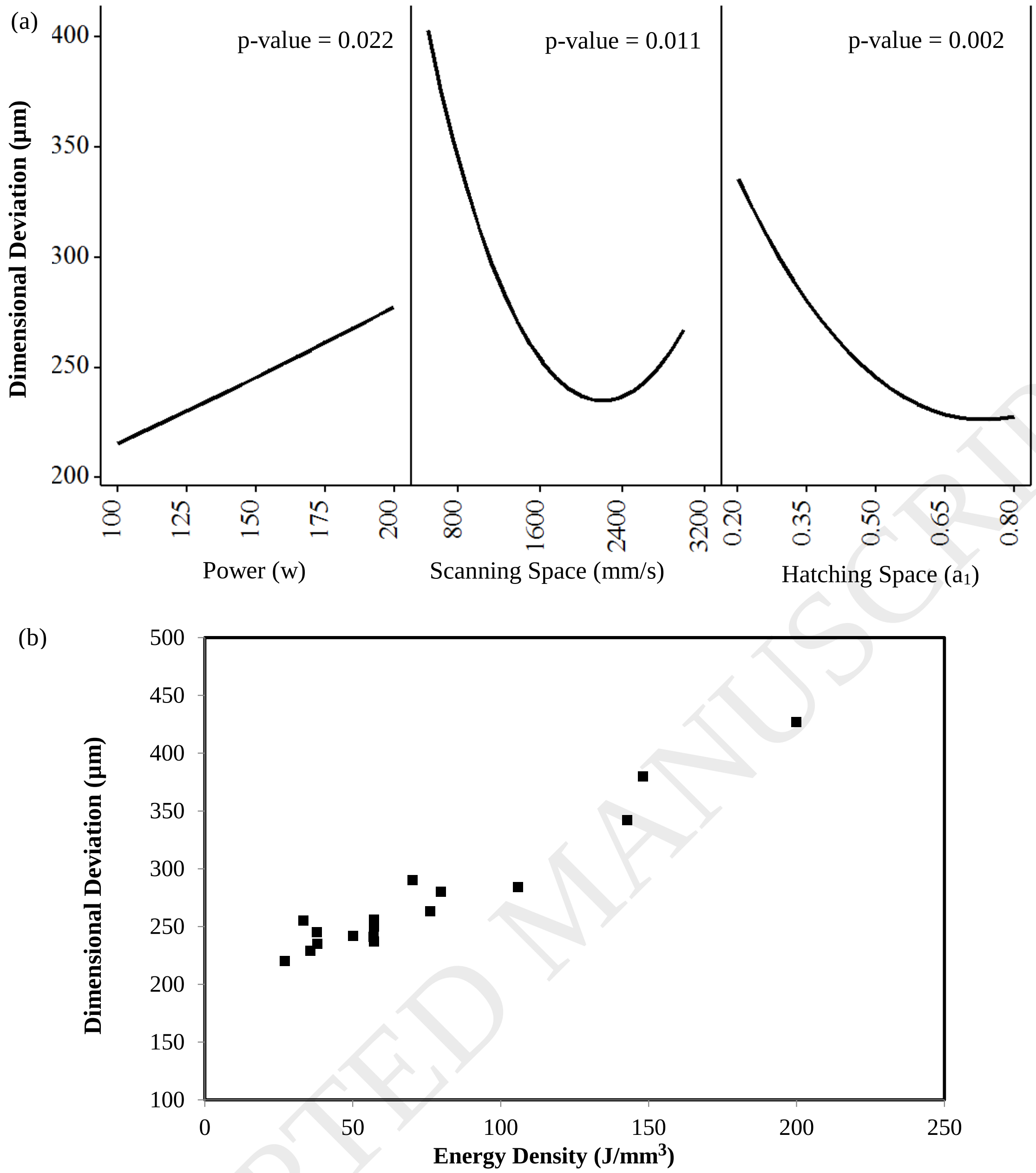

Figure 4: Effect of process parameters on the dimensional deviation.

Statistical analysis of dimensional deviation shows a clear dependence of this response on all the individual process parameters with p-values < 0.05. Parameters interactions were found less significant with high p-values. As shown in Figure 4 a, the dimensional deviation improves as the laser power and hatching spacing decrease. On the other hand, the dimensional deviation was reduced when the scanning speed increased until it reached about 2000 mm/s, whereas the dimensional deviation starts to increase again. Additional insight into the materials response can be gained by analysing the effect of the energy density on the dimensional deviation, see Figure 4 b. As described previously, the combined effect of the laser power, scan speed and scan spacing is represented by the energy density (J/mm^3); a semi-quantitative quantity that indicates the amount of laser input energy per unit volume. Figure 4 b shows that the dimensional deviation of the MCs consistently improves with decreasing the energy density, until achieving a minimum value of 220-235 μm at a range of energy densities 27 to 38 J/mm^3. Increasing the energy density causes the dimensional deviation to gradually deteriorate until it reaches its maximum when using energy density of 200 J/mm^3.

Figure 5 shows an example of the effect of the energy input on the effective diameter for MCs built with different orientations. For vertical MCs, it can be clearly seen that there is a decrease in the effective diameter with the increase in the energy density. This is because the track width increases with the increase in the energy input, which results in a decrease in the opening of the MCs. Unlike vertical MCs, the shape of the horizontal channels looks relatively elliptical as shown Figure 5. No horizontal MCs were obtained using high-energy input. This is because high-energy input penetrates deeper and melts several powder layers surrounding the MCs, which may block them. Similar results were also obtained for the inclined MCs. For low energy samples, the shape of the MCs with 500 µm intended design looks distorted. In addition, the use of high-energy input of 300 J/m^3 blocked all the MCs of any sizes.

It can be concluded that MCs built vertically had better dimensional deviation when compared to horizontal and inclined MCs. This is because the geometry of each slice built vertically was the same. As a result, vertical MCs appear identical because any building error is repeated for all the layers, generating more uniform edges, see Figure 5. On contrary, for the inclined and horizontal samples, the geometry of each slice depends on its position in the vertical direction. This leads to the accumulation of the building errors and hence distorts or blocks the MCs. In addition, the meltpool depth can go up to several layers, which has a significant impact on the topology of the inclined and horizontal MCs. This is in agreement with a study by White et al. who calculated the meltpool depth of AlSi10Mg during an SLM process and found that the depth of the meltpool is varied from 3-30 layers [40]. Another reason for the geometry deterioration of the horizontal and inclined MCs is the lack of support of the top surfaces, while no supports are needed for vertical MCs.

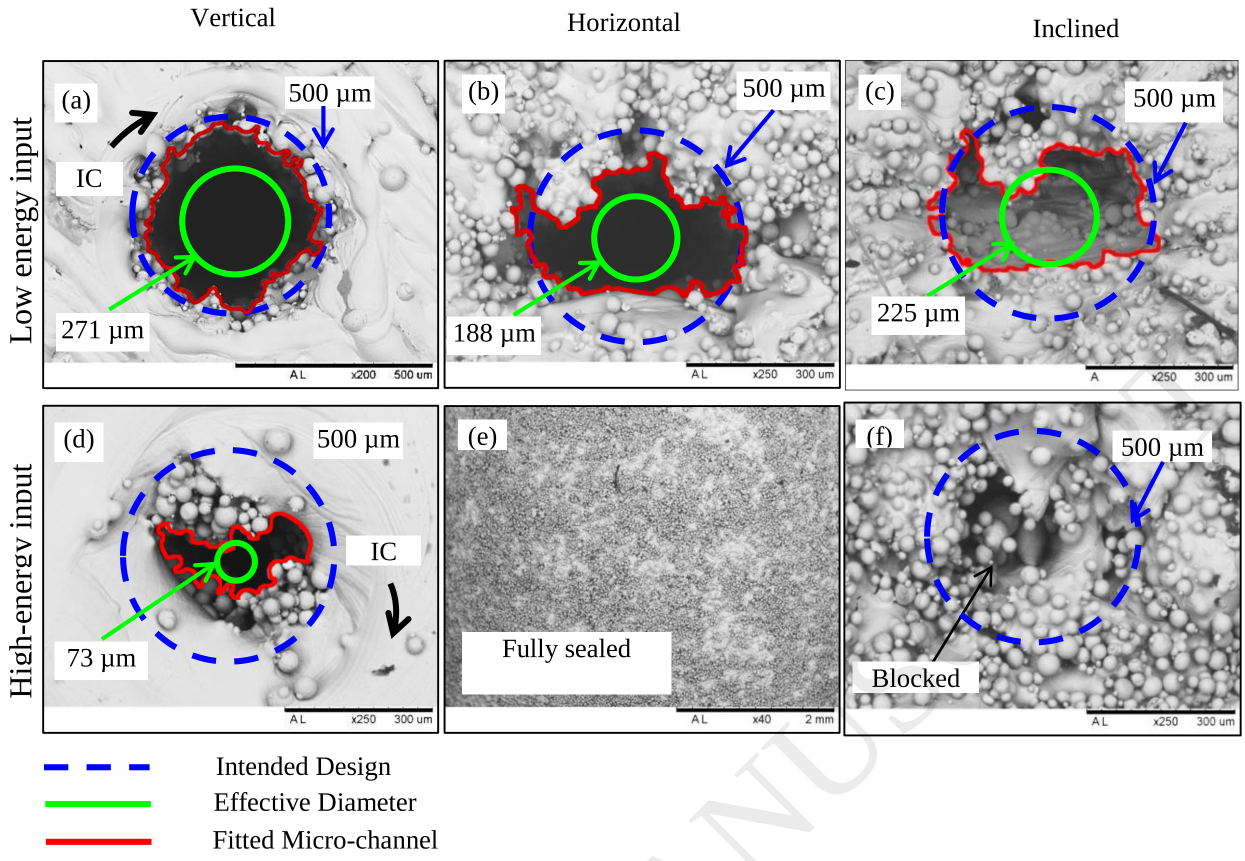

Figure 5: An example of vertical, horizontal and inclined 500 µm MC built with (a, b, c) low energy input of 35.7 J/mm^3 and (d,e,f) high energy input of 200 J/mm^3.

Figure 6a shows the individual effect of the laser power, scanning speed and the hatch spacing on the horizontal surface roughness. As shown in the figure, the horizontal surface roughness decreases insignificantly as the laser power increases. While it significantly decreases as the scanning speed decreases. On the other hand, the horizontal surface roughness initially increases when the hatching spacing increasing from 0.20 to about 0.60 then decreases as the scanning spacing increases further. Looking at the p-value of each individual parameter, it can be concluded that the scanning speed has a great significant whereas, the power and the hatching spacing are less significant. This is because the design space of the laser power has less impact on the overall energy density as it only varies from 100 w to 200 w, which is 2 times. On the other hand, the scanning speed varies from 500 mm/s to 3000 mm/s which is 6 times and the hatching spacing varies from 0.2 to 0.8 which is 4 times. In a study by *Qiu et al.*, the authors found that splashing and turbulence of melt pool observed using high speed camera were much pronounced when increasing the scan speed [41]. These explain why the melt pool becomes unstable with increased laser scanning speed.

Figure 6b shows the experimental results of the horizontal surface roughness with relation to the laser energy density. The figure shows that the horizontal surface roughness consistently improves with the increase of the energy density (increasing laser power, decreasing scanning space and hatching space). The minimum horizontal surface roughness of 1.45 µm was achieved using a high-energy input of 200 J/mm^3 while the highest horizontal surface roughness of 11.46 µm was obtained using a low energy input of 27 J/mm^3, see Figure 7. The increase of the laser energy density leads to the increase of the melt pool temperature enhancing the wetting behaviour, reducing balling and hence improves the surface roughness [42].

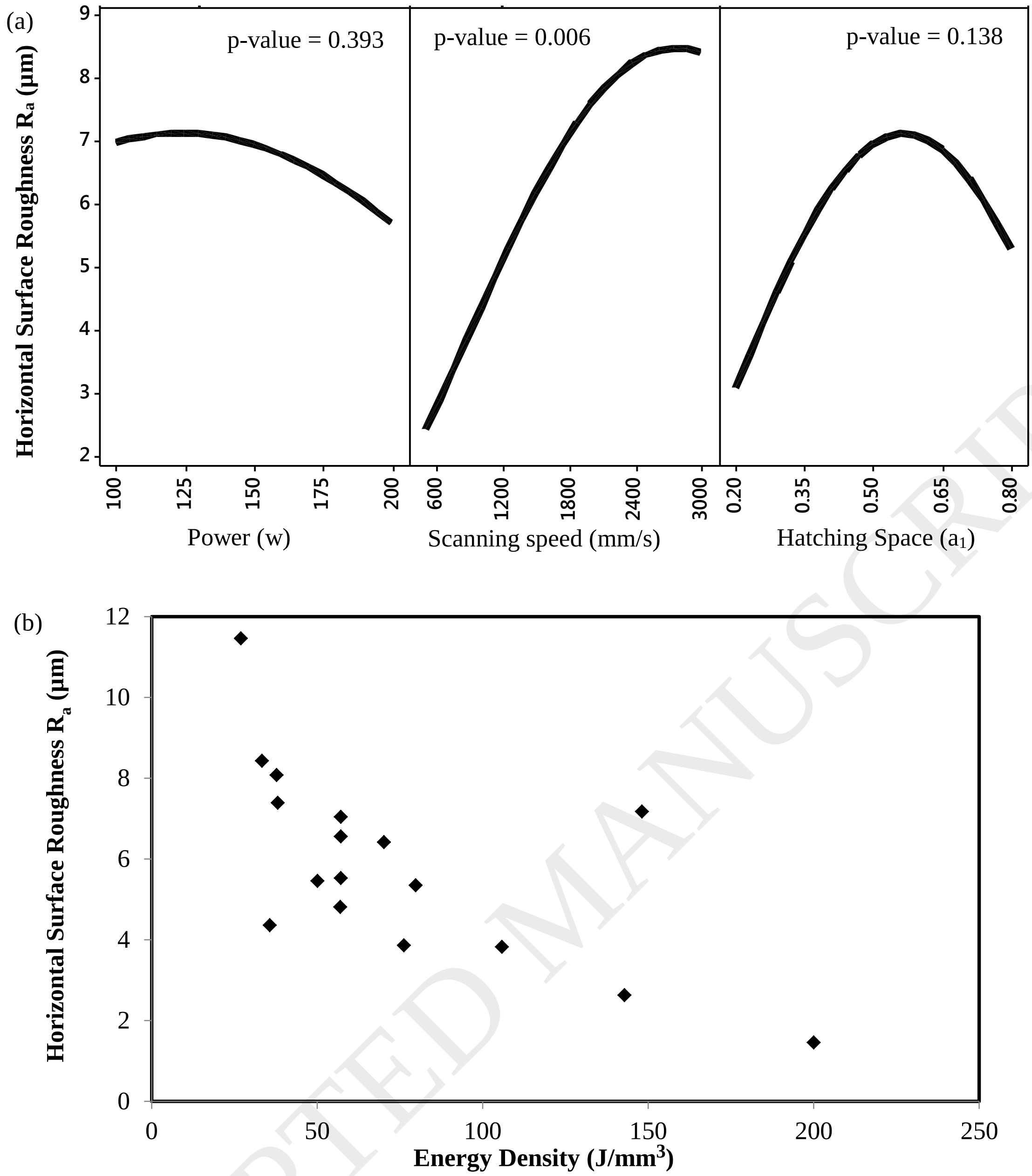

Figure 6: Effect of process parameters on the horizontal surface roughness.

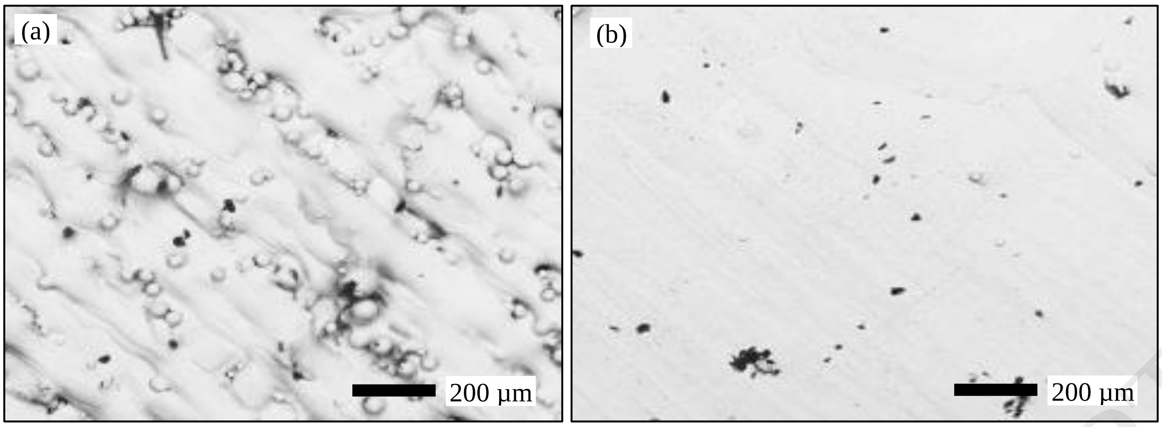

Figure 7: The horizontal surfaces of two samples fabricated with (a) low energy density of 35.7 J/mm^3 and (b) a high energy density of 200 J/mm^3. Note the balling morphology at the low energy density condition.

Figure 8a shows the effect of the process parameters on the vertical surface roughness. In general, there is insignificant improvement in the vertical surface roughness when varying the laser power and hatching spacing, whereas, less significant effect can be seen when varying the scanning speed. Figure 8b shows the experimental results of the vertical surface roughness in relation to the laser energy density. The figure confirms the weak dependency between the laser energy and the vertical surface roughness. Figure 9 shows SEM images of the lowest and highest vertical surface roughness samples. The figure reveals that the vertical surface roughness exhibit a larger amount of partially melt powder when compared to horizontal surface roughness, see Figure 7. This is because that the powder bed supports the vertical surfaces during the melting and solidification of the part layers. Therefore, powder particles close to the melt pool were partially melt and stuck to the vertical surfaces, see Figure 9. As reported by Jayasheelan *et al.* [43], the rough nature of the SLM samples is due to the presence of partially melted particles on the surfaces of the fabricated samples. On the other hand, Figure 9 does not show a significant difference in the surface topology of the two samples. Possibly because the difference in the surface roughness values of the two samples is not significant.

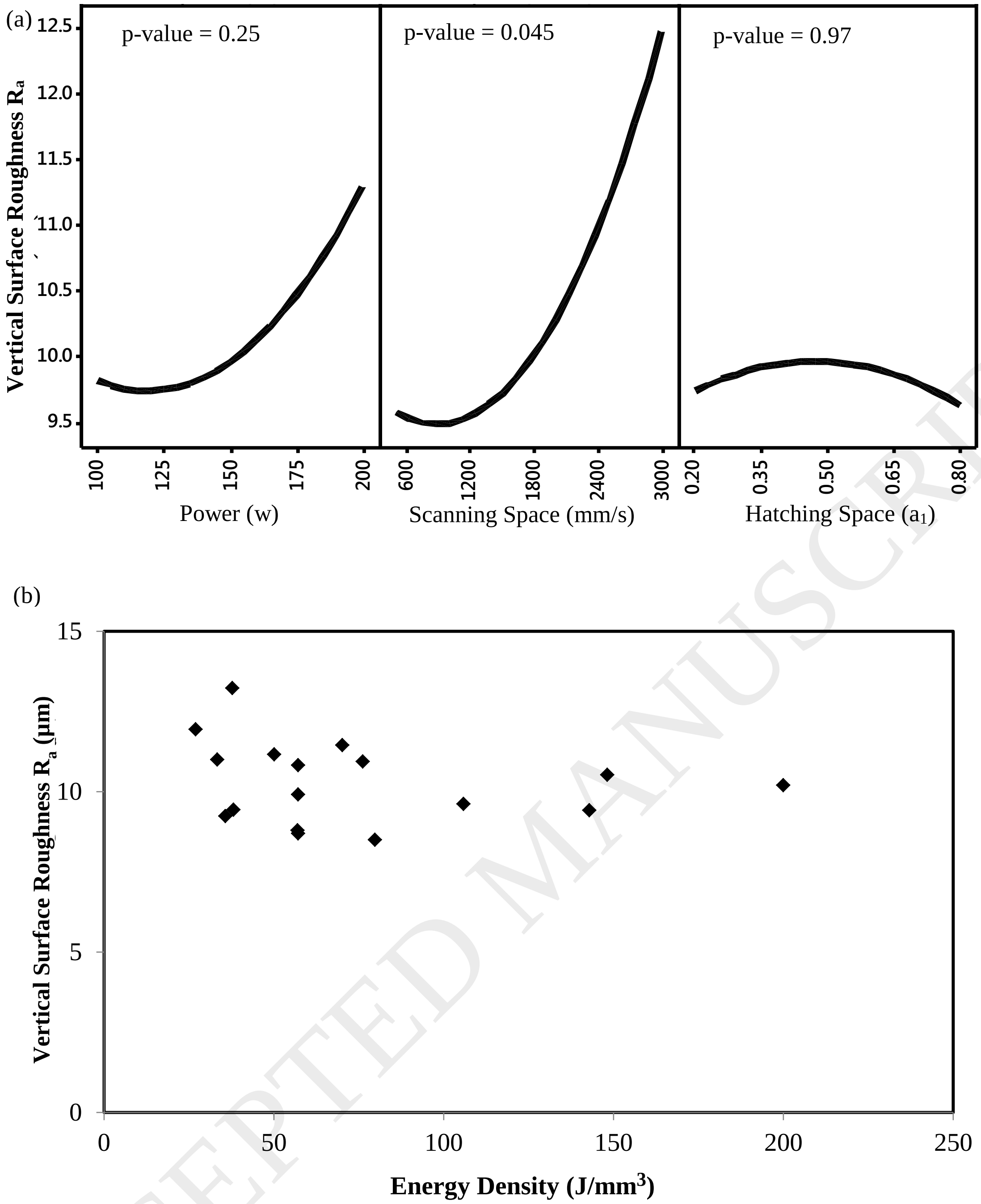

Figure 8: Effect of process parameters on the vertical surface roughness.

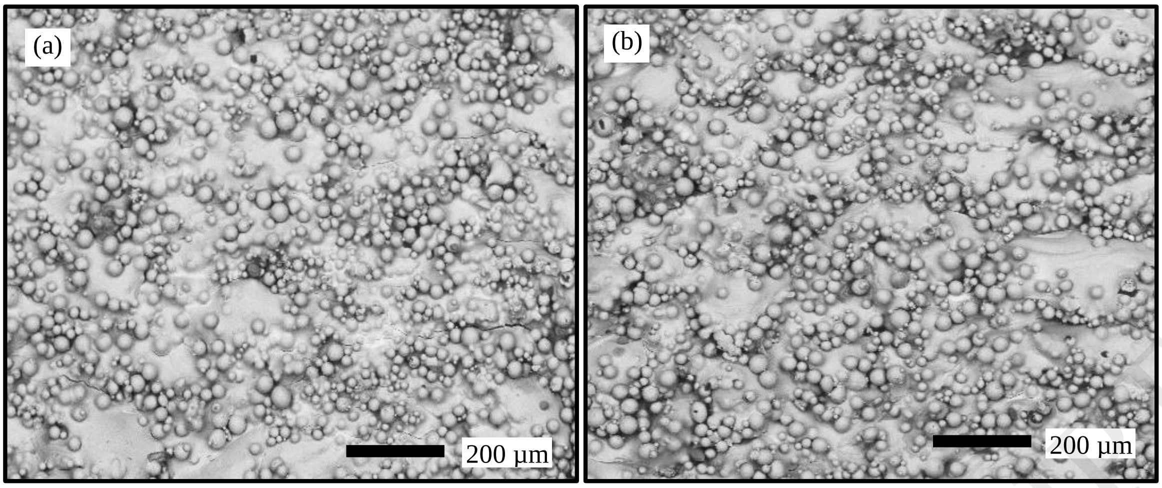

Figure 9: The vertical surfaces of the lowest and highest vertical surface roughness samples (a) R_a=8.5, energy density of 37.9 J/mm^3 and (b) R_a=13.23, energy density of 79.8 J/mm^3.

In summary, the experimental results indicate that vertical surface roughness cannot be significantly improved by optimising laser power, scanning speed or hatching spacing to meet the recommended biomedical implant roughness Ra= 1–2 µm [37]. Other parameters such as particle size distribution, layer thickness, and the position of the parts in the building platform have also shown to affect the vertical surface roughness [44-46]. Results from the horizontal surface roughness and the dimensional deviation of the MCs clearly indicate that an implant sample cannot simultaneously achieve an optimum dimensional deviation and horizontal surface roughness as shown in Figure 5 and Figure 7. As dimensional deviation improves when using low energy density the horizontal surface roughness, R_a worsens. The best horizontal surface roughness of 1.45 µm was achieved when using the highest energy density of 200 J/mm^3. However, using such high energy density resulted in deterioration in the geometry of the MCs and a low effective diameter of 73 µm was obtained for MCs with intended diameter of 500 µm. The best solution would be to optimise the process parameters with the best dimensional deviation using low energy density, followed by subsequent surface polishing to improve the surface quality.

3.3 MC Morphology

The presented results showed that the decrease in the laser energy density was more effective in producing samples with more accurate MCs that adhered most closely to the intended design. Therefore, samples 1, 5, 17 were selected for further investigation using MC morphology, Table 5. XCT imaging was used to support the choice of samples with the least dimensional deviation, while achieving minimum internal porosity. Further 3D analysis was performed to reveal the morphology of the channels and to calculate the internal residual porosity (open, closed and total) of the fabricated parts for the selected parameters. It was found that the lowest level of residual porosity belonged to samples 5. The printed MCs within the three samples were found to penetrate clearly into the reservoir region. As a result, the parameters used for manufacturing of samples 5 was selected and considered ideal for further investigation. Figure 11 illustrates the Ti-6Al-4V implant model manufactured via the optimum process parameters, which were used in the development of an antibiotic delivering orthopaedic implant (presented in our previous study) [10].

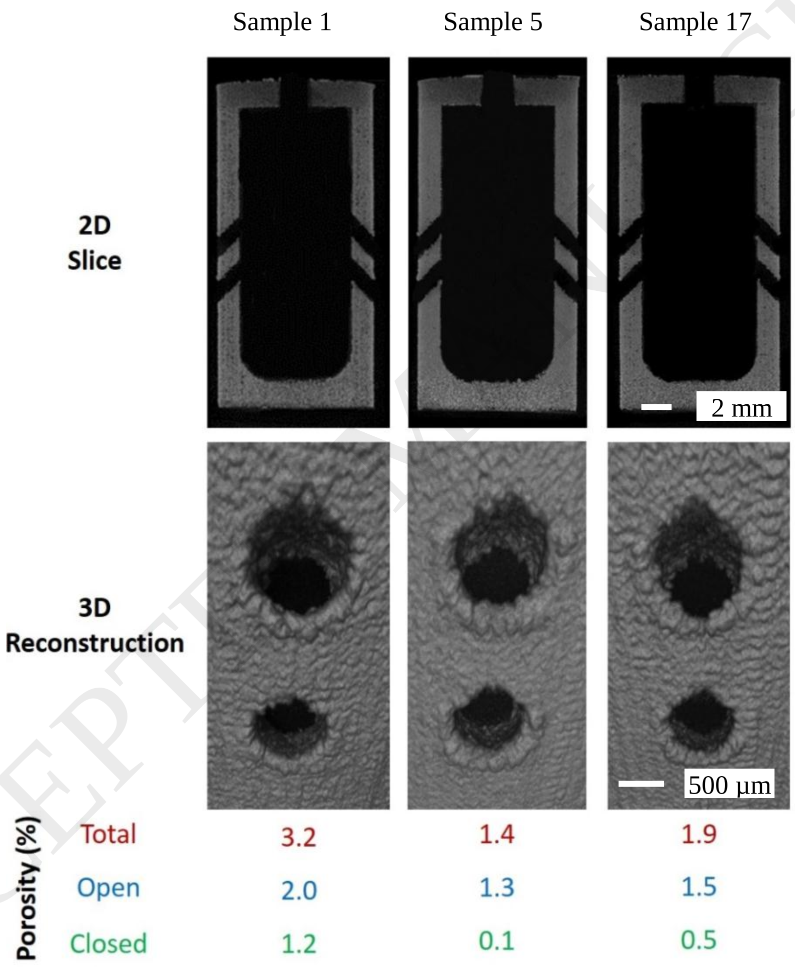

Figure 10: 2D binary images, 3D reconstruction and porosity measurements (total, open and closed) of the printed implant models with inclined pore orientation with three different process parameters indicating the MCs design were penetrated into the reservoir region.

Figure 11: Photograph of Ti-6Al-4V implant model manufactured via selective laser melting. As- fabricated part (right) and polished part (left).

4. Conclusions

The present study investigated the feasibility of tailoring SLM to manufacture Ti-6Al-4V samples with releasing-controlling MCs to be used as drug delivering implants. It was found that the build orientation and the internal contour of the MCs plays a key role in controlling the morphology and the effective diameter of the developed MCs. Vertical MCs with internal contour similar to the track width were found to have the least dimensional deviation from the target dimension of the MCs. The effect of the process parameters on the samples properties revealed that the dimensional deviation of the MCs and surface roughness of the samples could not be improved simultaneously. As the energy density was decreased, the dimensional deviation reduced, while the surface roughness worsened. Therefore, post-SLM polishing processes cannot be avoided in order to achieve the surface requirements of medical implants. The CT scan results identified the optimum processing parameters of samples with high accuracy releasing MCs and lowest porosity content. It was concluded that, samples with effective diameter of 229 µm and porosity of 1.4% could be obtained when using a low energy density of about 36 J/mm^3. Finally, although the aim of this work was to develop well-controlled releasing MCs for drug delivering implants, the results highlight the possibility of using the same approach to create dense parts with micro/macro channels for other applications, such as heat pipes and fluid devices.

Acknowledgements

The authors would like to acknowledge the Engineering and Physical Sciences Research Council (grant number EP/L020815/1) for funding this research.

References

[1] Global Health and Aging World Health Organization, 2011, p. 2.
[2] D. Tatkare, World Medical Implants Market Opportunities and Forecasts, Allied Market Research, Portland, United States, 2016, p. 66.
[3] J. Raphel, M. Holodniy, S.B. Goodman, S.C. Heilshorn, Multifunctional coatings to simultaneously promote osseointegration and prevent infection of orthopaedic implants, Biomaterials 84 (2016) 301-314.
[4] K.J. Bozic, S.M. Kurtz, E. Lau, K. Ong, V. Chiu, T.P. Vail, H.E. Rubash, D.J. Berry, The Epidemiology of Revision Total Knee Arthroplasty in the United States, Clinical Orthopaedics and Related Research® 468(1) (2010) 45-51.
[5] T.D. Kowalik, M. De Hart, H. Gehling, P. Gehling, K. Schabel, P. Duwelius, A. Mirza, The epidemiology of primary and revision total hip arthroplasty in teaching and nonteaching hospitals in the United States, Journal of the American Academy of Orthopaedic Surgeons 24(6) (2016) 393-398.
[6] M. Arruebo, N. Vilaboa, J. Santamaria, Drug delivery from internally implanted biomedical devices used in traumatology and in orthopedic surgery, Expert Opinion on Drug Delivery 7(5) (2010) 589-603.
[7] D. King, S. McGinty, Assessing the potential of mathematical modelling in designing drug-releasing orthopaedic implants, Journal of Controlled Release 239 (2016) 49-61.
[8] T. Kumeria, K. Gulati, A. Santos, D. Losic, Real-time and in Situ Drug Release Monitoring from Nanoporous Implants under Dynamic Flow Conditions by Reflectometric Interference Spectroscopy, ACS Applied Materials & Interfaces 5(12) (2013) 5436-5442.
[9] A.E.M. Eltorai, J. Haglin, S. Perera, B.A. Brea, R. Ruttiman, D.R. Garcia, C.T. Born, A.H. Daniels, Antimicrobial technology in orthopedic and spinal implants, World Journal of Orthopedics 7(6) (2016) 361-369.
[10] S.C. Cox, P. Jamshidi, N.M. Eisenstein, M.A. Webber, H. Hassanin, M.M. Attallah, D.E.T. Shepherd, O. Addison, L.M. Grover, Adding functionality with additive manufacturing: Fabrication of titanium-based antibiotic eluting implants, Materials Science and Engineering: C 64 (2016) 407-415.
[11] M. Gimeno, P. Pinczowski, M. Pérez, A. Giorello, M.Á. Martínez, J. Santamaría, M. Arruebo, L. Luján, A controlled antibiotic release system to prevent orthopedic-implant associated infections: An in vitro study, European Journal of Pharmaceutics and Biopharmaceutics 96 (2015) 264-271.
[12] A. Bégin-Drolet, M.-A. Dussault, S.A. Fernandez, J. Larose-Dutil, R.L. Leask, C.A. Hoesli, J. Ruel, Design of a 3D printer head for additive manufacturing of sugar glass for tissue engineering applications, Additive Manufacturing 15(Supplement C) (2017) 29-39.
[13] C. Qiu, N.J.E. Adkins, H. Hassanin, M.M. Attallah, K. Essa, In-situ shelling via selective laser melting: Modelling and microstructural characterisation, Materials & Design 87(Supplement C) (2015) 845-853.
[14] H. Hassanin, F. Modica, M.A. El-Sayed, J. Liu, K. Essa, Manufacturing of Ti–6Al–4V Micro-Implantable Parts Using Hybrid Selective Laser Melting and Micro-Electrical Discharge Machining, Advanced Engineering Materials 18(9) (2016) 1544-1549.

[15] A. Sabouri, A.K. Yetisen, R. Sadigzade, H. Hassanin, K. Essa, H. Butt, Three-Dimensional Microstructured Lattices for Oil Sensing, Energy & Fuels 31(3) (2017) 2524-2529.

[16] A. Uriondo, M. Esperon-Miguez, S. Perinpanayagam, The present and future of additive manufacturing in the aerospace sector: A review of important aspects, Proceedings of the Institution of Mechanical Engineers, Part G: Journal of Aerospace Engineering 229(11) (2015) 2132-2147.

[17] D.S. Thomas, S.W. Gilbert, Costs and cost effectiveness of additive manufacturing: A literature review and discussion, Additive Manufacturing: Costs, Cost Effectiveness and Industry Economics2015, pp. 1-96.

[18] B. Vayre, F. Vignat, F. Villeneuve, Metallic additive manufacturing: State-of-the-art review and prospects, Mechanics and Industry 13(2) (2012) 89-96.

[19] J.H. Tan, W.L.E. Wong, K.W. Dalgarno, An overview of powder granulometry on feedstock and part performance in the selective laser melting process, Additive Manufacturing 18(Supplement C) (2017) 228-255.

[20] M. Niinomi, K.I. Fukunaga, Gunawarman, G. Tono, J. Koike, D. Eylon, S. Fujishiro, Effect of microstructure on fracture characteristics of Ti-6Al-2Sn-2Zr-2Mo-2Cr-Si, Metallurgical and Materials Transactions A: Physical Metallurgy and Materials Science 32(11) (2001) 2795-2804.

[21] D.A. Puleo, A. Nanci, Understanding and controlling the bone-implant interface, Biomaterials 20(23-24) (1999) 2311-2321.

[22] R. Van Noort, Titanium: The implant material of today, Journal of Materials Science 22(11) (1987) 3801-3811.

[23] E. Sheydaeian, Z. Fishman, M. Vlasea, E. Toyserkani, On the effect of throughout layer thickness variation on properties of additively manufactured cellular titanium structures, Additive Manufacturing 18(Supplement C) (2017) 40-47.

[24] H. Galarraga, D.A. Lados, R.R. Dehoff, M.M. Kirka, P. Nandwana, Effects of the microstructure and porosity on properties of Ti-6Al-4V ELI alloy fabricated by electron beam melting (EBM), Additive Manufacturing 10(Supplement C) (2016) 47-57.

[25] L.E. Murr, S.M. Gaytan, F. Medina, H. Lopez, E. Martinez, B.I. MacHado, D.H. Hernandez, L. Martinez, M.I. Lopez, R.B. Wicker, J. Bracke, Next-generation biomedical implants using additive manufacturing of complex cellular and functional mesh arrays, Philosophical Transactions of the Royal Society A: Mathematical, Physical and Engineering Sciences 368(1917) (2010) 1999-2032.

[26] L.E. Murr, K.N. Amato, S.J. Li, Y.X. Tian, X.Y. Cheng, S.M. Gaytan, E. Martinez, P.W. Shindo, F. Medina, R.B. Wicker, Microstructure and mechanical properties of open-cellular biomaterials prototypes for total knee replacement implants fabricated by electron beam melting, Journal of the Mechanical Behavior of Biomedical Materials 4(7) (2011) 1396-1411.

[27] X.B. Su, Y.Q. Yang, P. Yu, J.F. Sun, Development of porous medical implant scaffolds via laser additive manufacturing, Transactions of Nonferrous Metals Society of China (English Edition) 22(SUPPL. 1) (2012) s181-s187.

[28] K.S. Chan, M. Koike, R.L. Mason, T. Okabe, Fatigue life of titanium alloys fabricated by additive layer manufacturing techniques for dental implants, Metallurgical and Materials Transactions A: Physical Metallurgy and Materials Science 44(2) (2013) 1010-1022.

[29] K. Sternberg, S. Petersen, N. Grabow, V. Senz, H.M. Schwabedissen, H.K. Kroemer, K.P. Schmitz, Implant-associated local drug delivery systems based on biodegradable polymers: Customized designs for different medical applications, Biomedizinische Technik 58(5) (2013) 417-427.

[30] N. Kurgan, Effect of porosity and density on the mechanical and microstructural properties of sintered 316L stainless steel implant materials, Materials & Design 55 (2014) 235-241.
[31] R. Fujisawa, M. Sakaihara, Y. Kurata, Y. Watanabe, Corrosion behaviour of nickel base alloys and 316 stainless steel in supercritical water under alkaline conditions, Corrosion Engineering, Science and Technology 40(3) (2005) 244-248.
[32] K.J. M. Imbaby, and I. Chang, Net shape fabrication of stainless-steel micro machine components from metallic powder, Journal of Micromechanics and Microengineering 18(11) (2008) 115018 (115017 pp.).
[33] S. Bender, V. Chalivendra, N. Rahbar, S. El Wakil, Mechanical characterization and modeling of graded porous stainless steel specimens for possible bone implant applications, International Journal of Engineering Science 53 (2012) 67-73.
[34] M.M. Dewidar, K.A. Khalil, J.K. Lim, Processing and mechanical properties of porous 316L stainless steel for biomedical applications, Transactions of Nonferrous Metals Society of China 17(3) (2007) 468-473.
[35] A. Bandyopadhyay, F. Espana, V.K. Balla, S. Bose, Y. Ohgami, N.M. Davies, Influence of porosity on mechanical properties and in vivo response of Ti6Al4V implants, Acta Biomaterialia 6(4) (2010) 1640-1648.
[36] F.E. Wiria, J.Y.M. Shyan, P.N. Lim, F.G.C. Wen, J.F. Yeo, T. Cao, Printing of Titanium implant prototype, Materials & Design 31, Supplement 1 (2010) S101-S105.
[37] L.P. Lefebvre, J. Banhart, D.C. Dunand, Porous Metals and Metallic Foams: Current Status and Recent Developments, Advanced Engineering Materials 10(9) (2008) 775-787.
[38] C.K.C. A. Liu, K.F. Leong, Properties of Test Coupons Fabricated by Selective Laser Melting, Key Engineering Materials 447-448 (2010) 780-784.
[39] F. Cardaropoli, V. Alfieri, F. Caiazzo, V. Sergi, Dimensional analysis for the definition of the influence of process parameters in selective laser melting of Ti–6Al–4V alloy, Proceedings of the Institution of Mechanical Engineers, Part B: Journal of Engineering Manufacture 226(7) (2012) 1136-1142.
[40] N.R. JP White, RM Ward, R Mellor, MM Attallah, Prediction of melt pool profiles for selective laser melting of AlSi10Mg alloy, Materials Science and Technology Conference and Exhibition,, Pittsburgh, 2014.
[41] C. Qiu, C. Panwisawas, M. Ward, H.C. Basoalto, J.W. Brooks, M.M. Attallah, On the role of melt flow into the surface structure and porosity development during selective laser melting, Acta Materialia 96(Supplement C) (2015) 72-79.
[42] M. Kamran, H. Neil, Top surface and side roughness of Inconel 625 parts processed using selective laser melting, Rapid Prototyping Journal 15(2) (2009) 96-103.
[43] J. Vaithilingam, E. Prina, R.D. Goodridge, R.J.M. Hague, S. Edmondson, F.R.A.J. Rose, S.D.R. Christie, Surface chemistry of Ti6Al4V components fabricated using selective laser melting for biomedical applications, Materials Science and Engineering: C 67 (2016) 294-303.
[44] A.A. Janvekar, M.A. Miskam, A. Abas, Z.A. Ahmad, T. Juntakan, M.Z. Abdullah, Effects of the preheat layer thickness on surface/submerged flame during porous media combustion of micro burner, Energy 122 (2017) 103-110.
[45] M. Król, T. Taski, Surface quality research for selective laser melting of TI-6AL-4V alloy, Archives of Metallurgy and Materials 61(3) (2016) 945-950.
[46] A.B. Spierings, N. Herres, G. Levy, Influence of the particle size distribution on surface quality and mechanical properties in AM steel parts, Rapid Prototyping Journal 17(3) (2011) 195-202.